



UNIVERSITY OF LEEDS

This is a repository copy of *Complex multifault rupture during the 2016 Mw 7.8 Kaikōura earthquake, New Zealand*.

White Rose Research Online URL for this paper:
<http://eprints.whiterose.ac.uk/113736/>

Version: Accepted Version

Article:

Hamling, IJ, Hreinsdóttir, S, Clark, K et al. (26 more authors) (2017) Complex multifault rupture during the 2016 Mw 7.8 Kaikōura earthquake, New Zealand. *Science*, 356 (6334). eaam7194. ISSN 0036-8075

<https://doi.org/10.1126/science.aam7194>

© 2017, American Association for the Advancement of Science. This is the author's version of the work. It is posted here by permission of the AAAS for personal use, not for redistribution. The definitive version was published in *Science* on 23 Mar 2017, DOI: 10.1126/science.aam7194.

Reuse

Items deposited in White Rose Research Online are protected by copyright, with all rights reserved unless indicated otherwise. They may be downloaded and/or printed for private study, or other acts as permitted by national copyright laws. The publisher or other rights holders may allow further reproduction and re-use of the full text version. This is indicated by the licence information on the White Rose Research Online record for the item.

Takedown

If you consider content in White Rose Research Online to be in breach of UK law, please notify us by emailing eprints@whiterose.ac.uk including the URL of the record and the reason for the withdrawal request.



eprints@whiterose.ac.uk
<https://eprints.whiterose.ac.uk/>

Complex multi-fault rupture during the 2016 Mw 7.8 Kaikōura earthquake, New Zealand

Authors: Ian J Hamling¹, Sigrun Hreinsdóttir¹, Kate Clark¹, John Elliott², Cunren Liang³, Eric Fielding³, Nicola Litchfield¹, Pilar Villamor¹, Laura Wallace^{1,4}, Tim J Wright², Elisabetta D'Anastasio¹, Stephen Bannister¹, David Burbidge¹, Paul Denys⁵, Paula Gentle⁶, Jamie Howarth¹, Christof Mueller¹, Neville Palmer¹, Chris Pearson⁵, William Power¹, Philip Barnes⁷, David J A Barrell¹, Russ Van Dissen¹, Robert Langridge¹, Tim Little⁸, Andrew Nicol⁹, Jarg Pettinga⁹, Julie Rowland¹⁰, Mark Stirling¹¹

Affiliations:

¹GNS Science, New Zealand.

²COMET, School of Earth and Environment, University of Leeds, Leeds, United Kingdom

³Jet Propulsion Laboratory, California Institute of Technology, Pasadena, CA, USA

⁴University of Texas Institute for Geophysics (UTIG), Austin, Texas, USA

⁵School of Surveying, University of Otago, Dunedin, New Zealand

⁶Land Information New Zealand (LINZ), Wellington, New Zealand

⁷National Institute of Water and Atmospheric Research, Wellington, New Zealand

⁸School of Geography, Environment and Earth Sciences, Victoria University of Wellington, Wellington, New Zealand

⁹Department of Geological Sciences, University of Canterbury, Christchurch, New Zealand

¹⁰School of Environment, University of Auckland, Auckland, New Zealand

¹¹Geology Department, University of Otago, Dunedin, New Zealand

*Correspondence to: I.Hamling@gns.cri.nz

Abstract: On 14th November 2016, the northeastern South Island of New Zealand was struck by a major Mw 7.8 earthquake. Field observations, in conjunction with InSAR, GPS, and seismology reveal this to be one of the most complex earthquakes ever recorded. The rupture propagated northward for more than 170 km along both mapped and unmapped faults, before continuing offshore at its northeastern extent. Geodetic and field observations reveal surface ruptures along at least 12 major faults, including possible slip along the southern Hikurangi subduction interface, extensive uplift along much of the coastline and widespread anelastic deformation including the ~8 m uplift of a fault-bounded block. This complex earthquake defies many conventional assumptions about the degree to which earthquake ruptures are controlled by fault segmentation, and should motivate re-thinking of these issues in seismic hazard models.

One Sentence Summary: Major earthquake rips through evolving fault zone, defying conventional wisdom regarding the degree of fault segmentation during earthquake ruptures.

Main Text:

Introduction

Whether or not multiple fault segments can rupture during a single earthquake is critical for our understanding of seismic hazard and potential maximum earthquake magnitudes. Variations in stress levels along a rupture and geometric complexities, such as fault step overs, are thought to be a primary control of final rupture length (1,2). While numerical models and field observations suggests that fault step overs of more than 4-5 km can halt a ruptures' propagation (1,3,4), near-instantaneous triggering over distances of more than 50 km has been documented (5, 6).

Furthermore, recent observations indicate that fault networks with both optimally oriented and misoriented faults can rupture during a single earthquake (7, 8). Insights from complex ruptures involving multiple faults, including the 2010-2011 Christchurch earthquake sequence in New Zealand (9) and El Mayor-Cucupah in Mexico (7, 8) are starting to feed into seismic hazard models relaxing some of the assumptions surrounding fault segmentation and multifault ruptures (10).

Here we show detailed geodetic and geological evidence of highly complex fault rupture during the 14 November 2016 (13th November 11:02 UTC) Mw7.8 Kaikōura earthquake in the northern South Island of New Zealand. The earthquake resulted in surface slip of more than 10 m along multiple faults, several of which were previously unmapped or considered inactive (Figure 1), despite NZ having one of the most accurate and comprehensive maps of active faulting worldwide (11). The earthquake ruptured faults across two distinct seismotectonic domains, with fundamentally different characteristics (12), a scenario which would have been excluded from seismic hazard models.

Oblique convergence between the Pacific and Australian plates at rates of 39-48 mm/yr (13) dominates New Zealand's tectonics. In the North Island, relative plate motion is mostly accommodated by subduction along the Hikurangi subduction zone (14, 15), while central South Island tectonics is dominated by dextral transpression on the Alpine Fault (13). The strike-slip dominated Marlborough Fault System (MFS, Figure 1) in the northern South Island occupies the transition from Hikurangi subduction to the strike-slip dominated Alpine Fault (16, 17). South of the MFS, in the Northern Canterbury region, active deformation is dominated by transpression, distributed among a number of slowly deforming faults and folds, including the Humps and Hundalee faults (18). Although the southern end of the subducting Pacific slab underlies the MFS at depths of 25-30 km (19), Quaternary and geodetic strain (16,17,20) suggest that the majority (>75%) of the relative plate motion within the northern South Island is accommodated at the surface by faults in the MFS. Slip rates through the MFS decrease from south to north. The northern most faults, the Awatere, Clarence and Wairau have slip rates in the range of 4 to 8 mm/yr (21-23). In contrast, some of New Zealand's fastest-slipping onshore faults at the southeastern edge of the MFS: the Hope and Kekerengu faults have Quaternary slip rates varying from 18 to 25 mm/yr (20, 24-26). As the Hope Fault approaches the coastline, it transfers much of its slip to the Jordan Thrust, which has a more northerly strike (and hence a larger reverse component). Further north, the Jordan Thrust slip is transferred to the mostly dextral strike-slip Kekerengu fault in the northeastern South Island (12, Figure 1).

The 14th November 2016 Kaikōura Earthquake

The Mw 7.8 Kaikōura earthquake struck just after midnight on 14th November with an epicenter ~20 km south of the Hope Fault (Figure 1). The earthquake was the most powerful experienced in that area in more than 150 years. Shaking was widely felt throughout New Zealand with widespread damage occurring across the northern South Island. Global moment tensor solutions showed a combination reverse and strike slip faulting with a strong non-double couple component. Aftershocks follow a broad NE-SW trend proximal to the Humps and Hundalee faults for ~80 km extending offshore near Kaikōura (Figure 1, S1). The aftershocks then step north, approximately following the Jordan Thrust and Kekerengu faults, with a large cluster of events occurring in the Cape Campbell and Lake Grassmere area (Figure 1), the site of a Mw 6.8 earthquake in 2013 (27). Regional moment tensors (28) for aftershocks show a mixture of reverse and strike slip mechanisms with the majority of events occurring in the upper 20 km (Figure S1). The earthquake generated a tsunami (up to 3 m at Kaikōura) which was detected at four tide gauges along the east coast of both the North and South Islands. We used marigrams from these tide gauge stations to determine the travel times of the first arrivals of the tsunami wave field located at Kaikōura (0.11 h), Castlepoint (0.83 h), Wellington (0.95 h) and Christchurch (1.53 h). Simple travel time inversion assuming reciprocity between the source of the tsunami and the location of the tide gauges places the source of the tsunami in the coastal area ranging from just south of Kaikōura northwards to Cape Campbell (Figure 1, S2), which corresponds to the general area of coastal uplift.

Field observations following the earthquake record major (meter-scale) ground surface ruptures on some or all of at least 12 transpressional faults (Figure 1). In the North Canterbury region, near the epicenter, two previously identified ENE to NE-striking faults displayed oblique metre-scale, up-to-the-NW, surface rupture of as much as 2 m, with similar dextral strike-slip (The Humps Fault Zone) and subordinate strike-slip (Hundalee Fault). In addition, there was oblique dip-slip sinistral strike-slip surface rupture of typically ~1 m on at least two previously unidentified N to NNW-striking faults. The Hundalee Fault rupture extended across the coast and offshore, with its NW-upthrown side marking the southern limit of recognizable coseismic coastal uplift (see below). Within the MFS, metre-scale dextral strike-slip surface rupture occurred on at least five NE-striking structures: the Upper Kowhai Fault, Jordan Thrust, Fidget Fault, Kekerengu Fault and the offshore Needles Fault. The largest displacements documented so far on the onshore NE-striking faults are 12 m dextral offset on the Kekerengu Fault with ~1-3 m of vertical offset, and as much as 4 m dextral offset on the Jordan Thrust. Perhaps the largest surprise was the large amount of surface displacement on the NNW-striking oblique reverse-sinistral Papatea Fault, with as much as 5-6 m strike-slip and 6-7 m dip-slip. Minor (<0.5 m), surface displacements were observed on two faults near Cape Campbell, and on the Hope Fault, where it meets the coast.

Uplift observed along the Kaikōura coast was highly variable with field measurements ranging from 0.6 to 4.8 m (Figures 2). No coastal change was observed south of the Hundalee Fault, but on the northern side of the fault there was coastal uplift of 1.6 ± 0.3 m. The amount of uplift decreased northward toward Kaikōura Peninsula, which was uplifted ~0.9 m. Coastal uplift remained low for approximately 12 km north of Kaikōura Peninsula before increasing to ~2 m of

uplift south of the Hope Fault. Between the Hope Fault and the Papatea Fault coastal uplift was relatively high at $\sim 2 - 3$ m. Maximum coastal uplift of 4.8 ± 0.5 m occurs on the 700 m-wide block between the two fault strands of the Papatea Fault. There appeared to be little or no uplift between the Kekerengu and Papatea faults. Consistent uplift of $2.5 - 3$ m was measured inboard of the mapped segments of the onshore Kekerengu Fault and the submarine Needles Fault, confirming continuous submarine fault rupture between these two faults.

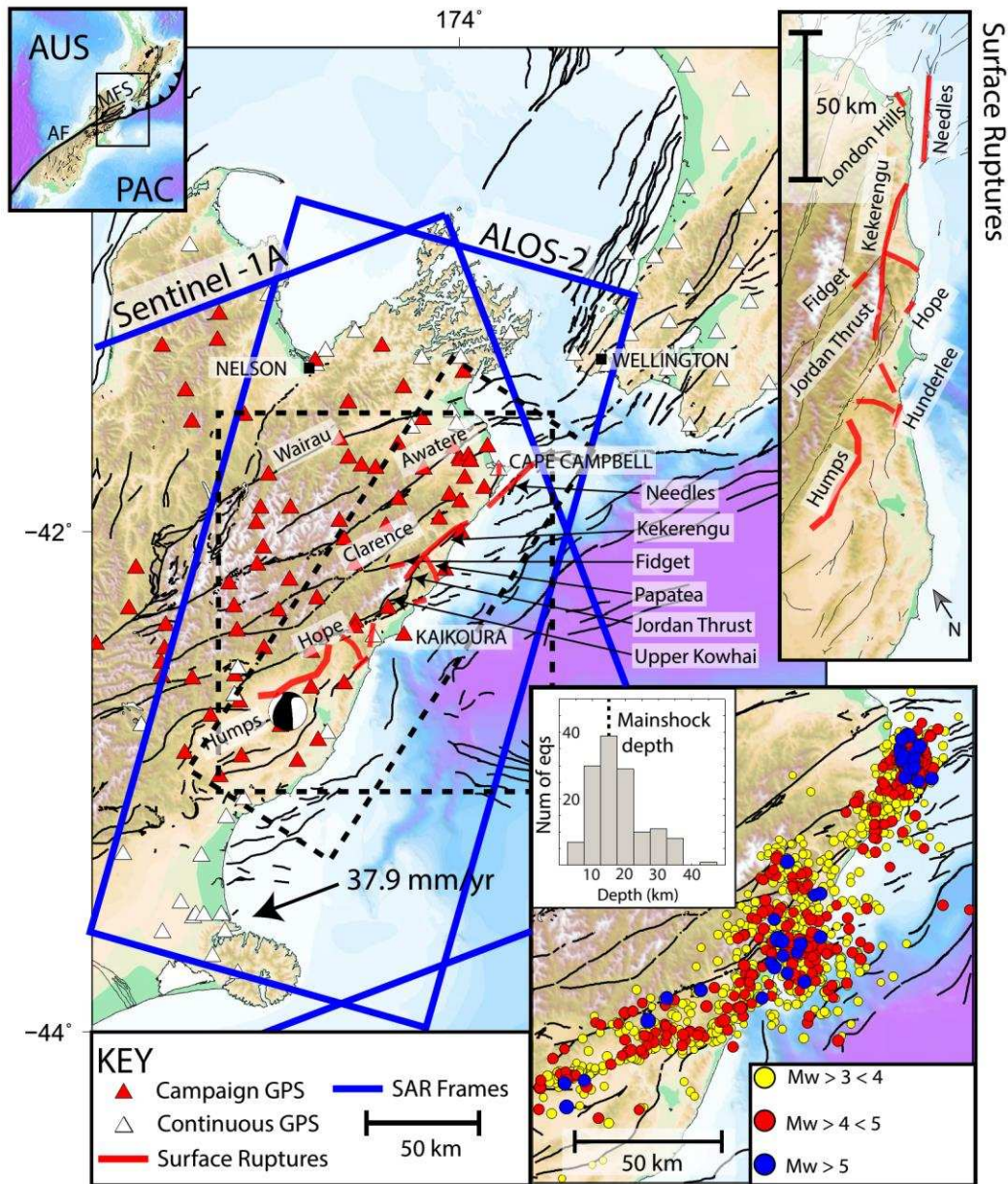


Figure 1. Color shaded relief of central New Zealand. The main figure shows the location of the continuous (white triangles) and campaign (red triangles) GPS sites. Heavy blue lines indicate the frame boundaries for the Sentinel-1a and ALOS-2 InSAR frames used in the study and red lines show the location of surface rupturing. The lower case labels denote some of the major crustal faults running through the MFS and the upper case labels show the towns/cities of

Kaikoura, Wellington and Nelson and the Cape Campbell region. The dashed black boxes indicate the regions shown by the two sub-figures. The vector shows the relative plate motion between the Pacific (PAC) and Australian plates (AUS) as indicated in the top left. The beach ball gives the W-phase moment tensor generated by the USGS at the epicentral location. Bottom right: Distribution of relocated aftershocks over magnitude 3 occurring in the first 2 weeks. Earthquakes are color coded by magnitude. The histogram shows the depth distribution of Mw 4.5 and above. Top right: Map showing the regions with observed surface ruptures (red lines).

Continuous and campaign GPS data (29) recorded displacements with more than 6 m of lateral motion in the vicinity of Cape Campbell (Figure 1, 2) and uplift of up to 2 m at the northern end of the Seaward Kaikōura mountain range (Figures 2). Widespread uplift is also observed in the vicinity of Kaikōura with areas of subsidence found inland of the Clarence Fault and to the south of the Humps and Hundalee faults in North Canterbury (Figure 1, 2). Two sites, located to the south of the Kekerengu Fault, show westward motion of ~2 m consistent with the right-lateral offsets. In addition to GPS data, Synthetic Aperture Radar (SAR) data were acquired by the European (ESA) and Japanese (JAXA) Space Agency's Sentinel and ALOS-2 missions respectively (Table S1, S3). Both ascending (Sentinel-1A, ALOS-2) and descending (ALOS-2) interferograms corroborated many of the early field observations but also revealed a much more complex fault rupture than was initially realized. Both the ascending and descending interferograms retain good coherence across most of the region with maximum line-of-sight (LOS) changes of ~1.3 m in the ascending and ~-3 m in the descending tracks (Figures 3, S4). There is some loss of coherence along the coast and close to many of the ground ruptures. This is a result of large phase gradients in the nearfield, extensive landslide activity and changes to the ground surface.

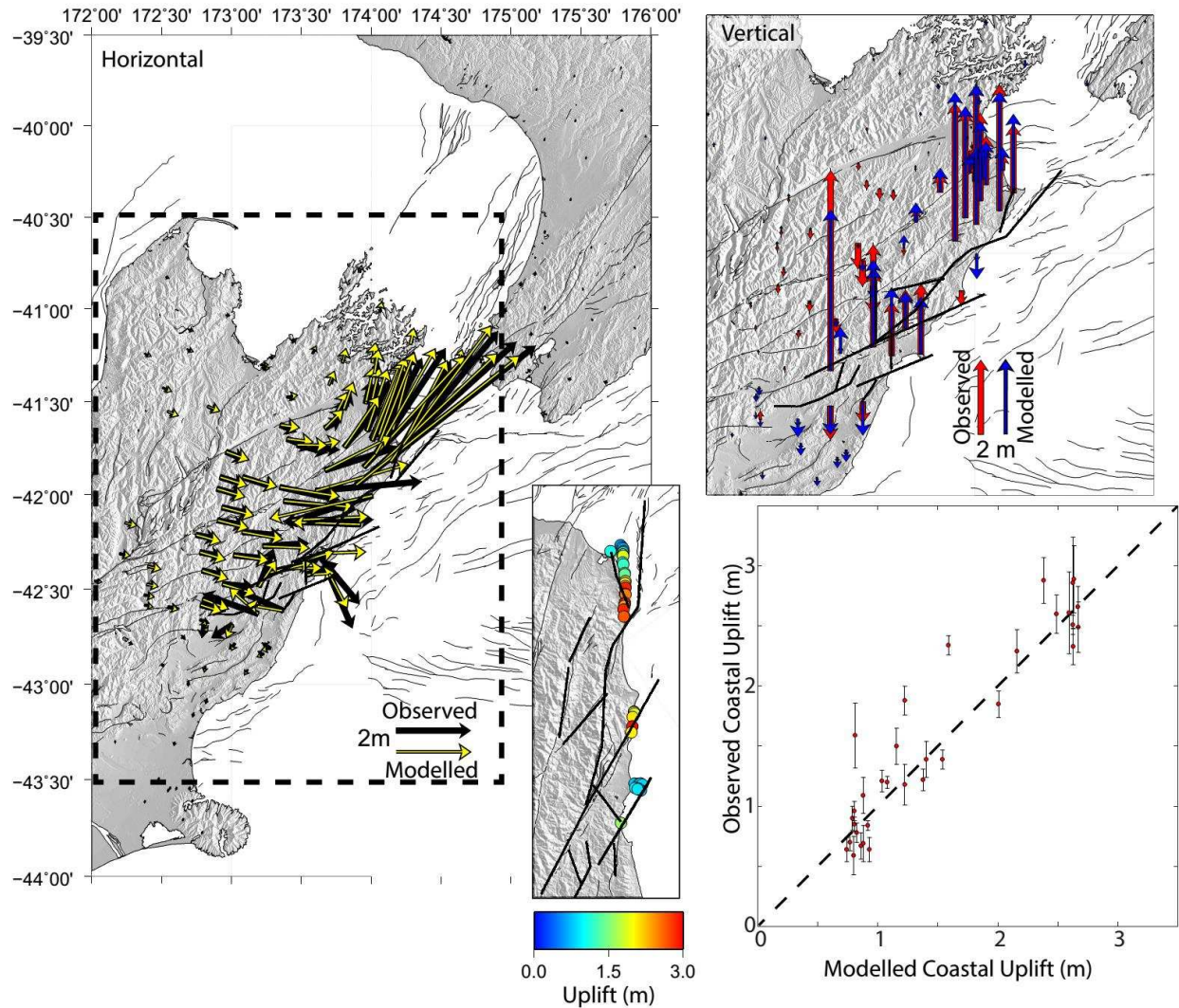


Figure 2: Observed (black) and modelled (yellow) horizontal displacements at continuous and campaign GPS sites assuming only crustal faulting. The black dashed line indicates the region shown in Figure 3. Observed and modelled vertical displacements are shown in as red and blue arrows respectively. Coastal uplift observations are indicated by the colored circles and a comparison between the observed and modelled uplift is shown in the bottom right. The dashed line shows correlation of $R = 1$.

The Sentinel-1 and ALOS-2 images reveal the largest displacements in two distinct regions. In the south, deformation is concentrated along an NE-SW trend running along The Humps Fault Zone and towards the Hundalee Fault (Figures 3, S4). The deformation then steps north where it broadens inland from Kaikōura consistent with slip along the Upper Kowhai Fault, Jordan Thrust and onto the Kekeurangi Fault as observed in the field (Figure 3). In addition to the InSAR data, Multi-Aperture InSAR (MAI) and range and azimuth offsets, which do not suffer from decorrelation in the nearfield, show a number of sharp discontinuities which match with ground observations (Figures S4). Using the range and azimuth offsets from the ascending and an additional descending Sentinel pair (note that the phase data is not used due to the long temporal

baseline) we also generated a full 3D displacement field (Figure 4, 29). The radar derived displacement field shows good agreement with the GPS and geological field observations (Figure 4). Across the Kekepengu Fault there are horizontal displacements of ~ 10 m with hanging wall uplift. Some of the largest deformation is observed in a 50 km^2 region south of the convergence point between the Jordan Thrust, and the Kekepengu and Papatea faults, which has been uplifted by up to 8 m and translated south by 4-5 m (Figure 4). Both the satellite-derived deformation and field observations show a seaward decrease in the amount of uplift and left-lateral offsets along the Papatea Fault. In the vicinity of the epicenter, there are two discrete regions of uplift between The Humps Fault Zone and the Hope Fault. This is also observed in the MAI offsets (Figure S4) which show NNE-SSW discontinuities associated with slip at depth. Scattered N-S trending, sinistral-reverse surface ruptures, mapped in the field in association with both faults, could be accommodating some of the uplift but their displacements do not account for the uplift detected by InSAR.

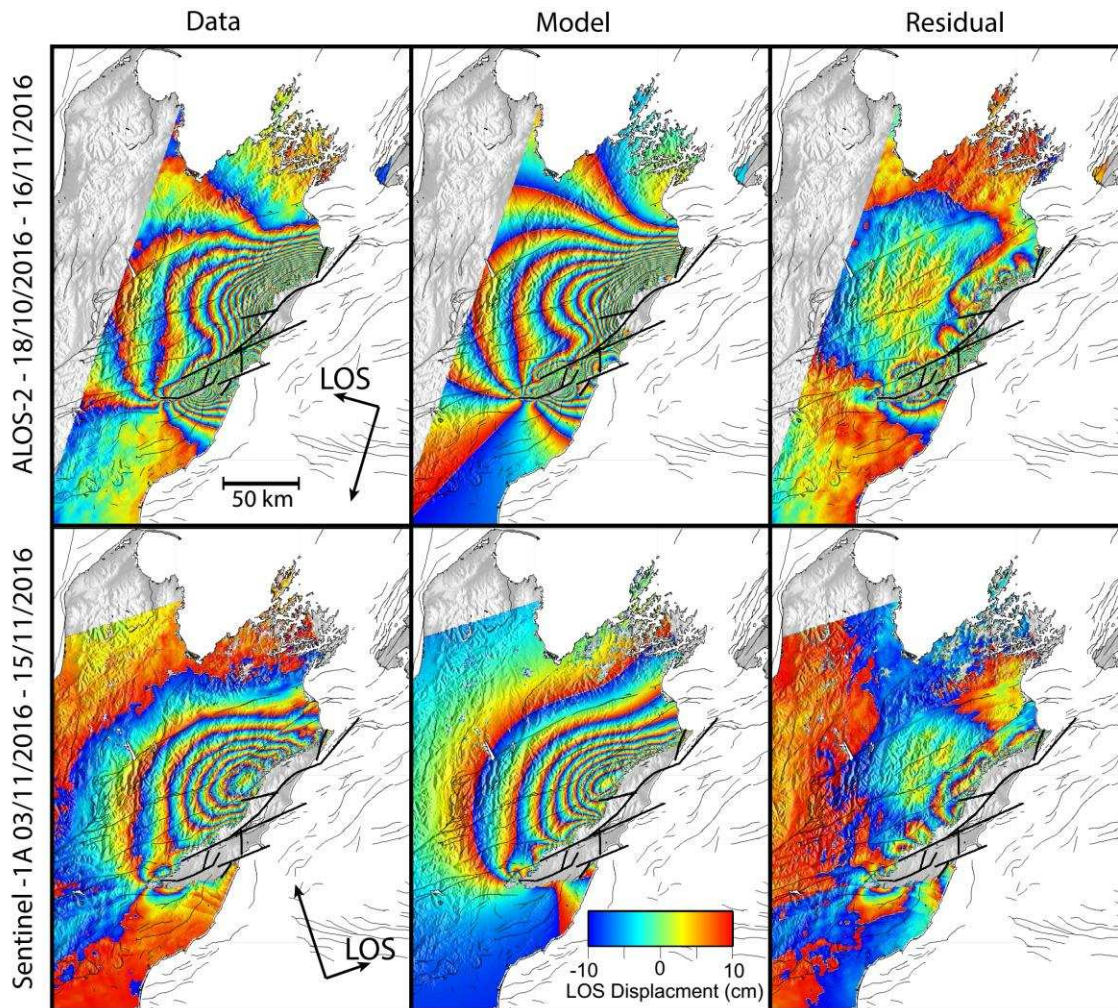


Figure 3: Observed, modelled and residual interferograms based on the best fit model shown in Figure 5. Heavy black lines indicate the fault patches modelled to have slipped during the earthquake.

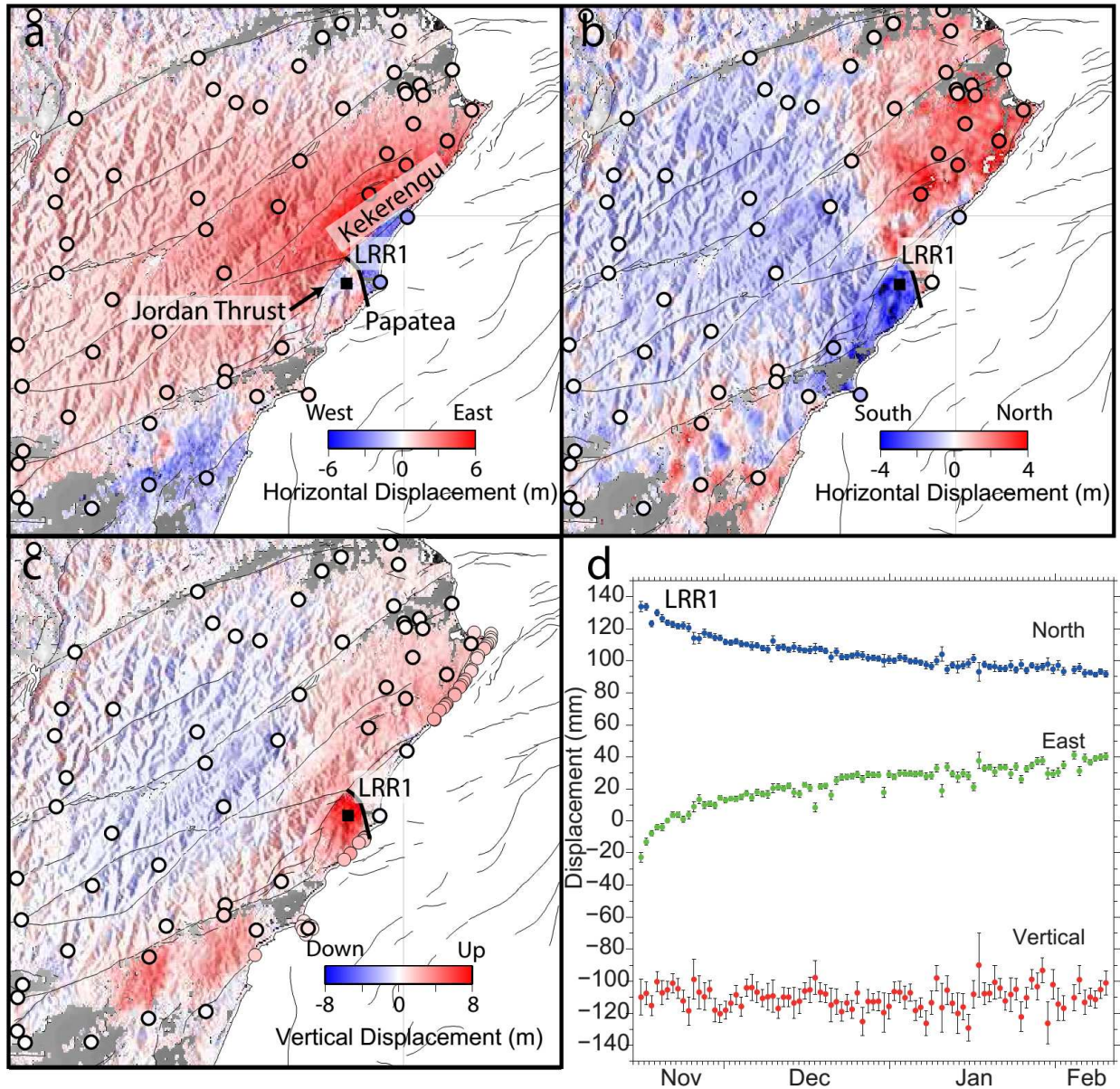


Figure 4: 3D displacement field derived from Sentinel-1A ascending (03/11/2016 – 15/11/2016) and descending (05/09/2016 – 16/11/2016) azimuth and range offsets (29). a) East-West displacements, thin black lines show the location of mapped active faults and the circles show the equivalent displacements at GPS sites with the same color scale, heavy black line shows the location of the Papatea fault. b) North-South displacements. The circles show the equivalent displacements at GPS sites with the same color scale. c) Vertical displacements. The circles show the equivalent displacements measured along the coast and at GPS sites (heavy outlines) with the same color scale d) North, east and vertical post-seismic displacement time-series from a semi-continuous GPS (LRR1) installed southwest of the Papatea Fault on 16th November (black square in a, b and c)

Deformation Modeling

To develop a slip model for the earthquake, we have used the ascending and descending phase data, coseismic offsets from 226 continuous and campaign GPS sites from the South and North Islands. Although a number of additional scenes have been acquired by the Sentinel and ALOS-2 satellites since the earthquake, to minimize the effects of post-seismic deformation and aftershocks we used only the earliest co-seismic pairs which were both acquired on 15th November, approximately 24-36 hours after the mainshock. We fixed the dip of each fault to their geologically estimated values (12) and discretize each fault into ~ 2 by ~ 3 km patches along strike and downdip respectively assuming a constant dip (29). The fault geometry is constrained based on discontinuities observed in the InSAR data, including azimuth and range offsets, and field observations of coastal uplift (Figures 3, S4). The earthquake is modelled as a set of rectangular dislocations in an elastic half space (30). The deformation pattern observed around the Papatea Fault could not be fit using an elastic model (such as ours), and we expect that most of the deformation associated with the Papatea block is related to anelastic deformation within a fault restraining bend (see discussion). For this reason, we do not include the Papatea Fault in our slip inversions, and data around the uplifted block was removed. We fixed the depth to the base of each fault to 25 km, and solved for the slip and rake direction of each fault patch using a nonnegative least-squares inversion (29, 31).

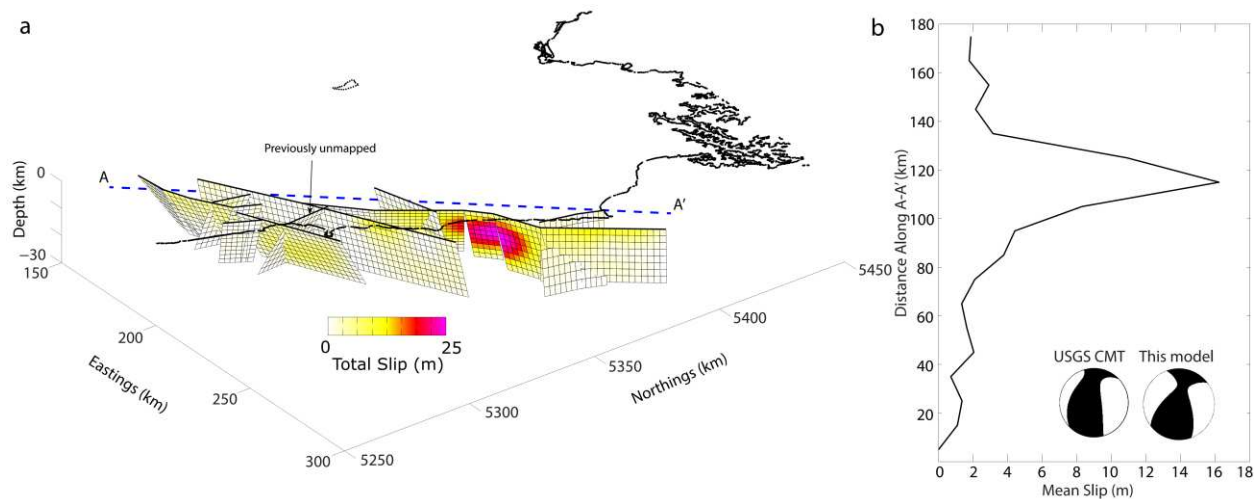


Figure 5. Best fitting crustal fault model for the Kaikōura earthquake. **a)** Best fitting slip distributions based on the inversion of geodetic and coastal uplift data. Heavy black lines denote the top edge of the fault surface. Arrow indicates a previously unmapped fault running between the Hundalee and Hope Faults **b)** Average slip along profile A-A' indicated by the blue line shown in **a** and **c**. The beach balls show a comparison between the USGS CMT solution and the equivalent solution generated by this model.

The best fit crustal fault model, which explains more than 95% of the subsampled data variance (88 and 85 % for full resolution ascending and descending data excluding the region around the Papatea block), involves slip along multiple fault segments with a combination of strike-slip and reverse faulting (Figure 5, S5). The model gives a total moment equivalent to a Mw 7.9 earthquake, using a shear modulus of 30 GPa, consistent with the global estimates of Mw 7.8, although the moment tensor based on the geodetic inversion shows a larger strike-slip

component than that estimated from global seismology data (Figure 5b). In the epicentral region, we obtained slip of up to 6 m of dextral and reverse slip at depths of ~5 – 25 km on The Humps Fault Zone and Hundalee Fault with 2-3 m near the surface compatible with the field observations. In total, the cumulative moment from the faults in North Canterbury equates to a Mw 7.5 earthquake. Near the coastal end of the Hundalee Fault, discontinuities observed in the InSAR data suggest a more north-south trending fault running between the Hundalee and Hope faults. Here we estimate ~1.5 m of mostly reverse slip extending over much of the modelled fault plane. On the seaward part of the Hope Fault we predict localized slip of almost 8 m in the upper 3 km with 2 m of slip at depth. However, limited data and local inelastic effects makes this poorly constrained. The 3D displacements (Figure 4) and field data acquired in the vicinity shows no more than 0.2 m of horizontal displacement on this portion of the Hope Fault suggesting that our inversion is allocating too much shallow slip to the seaward portion of the Hope Fault. To the north, where the largest fault offsets are observed in the field, we estimate up to 25 m of strike-slip and 9 m of reverse slip along the Jordan Thrust and Kekerengu Fault at depths of between 10 and 25 km decreasing to ~10 m near the surface. Along the submarine Needles Fault, we estimated strike-slip of up to 10 m in the upper 10 km with shallow reverse slip of ~5 m (Figure S5). In summary, the rupture propagated through two distinct tectonic domains separated by a major left-stepping discontinuity centered on the Papatea block. Our slip model for crustal faults indicates that faults in the North Canterbury domain have a greater reverse component and yield an average rake of 130° compared to those of the MFS which have greater dextral slip with an average rake of $\sim 160^\circ$.

Discontinuities in the InSAR data and field observations indicate that a number of smaller fault strands also slipped during the rupture including the London Hills and Fidget faults (Figure 1). We estimated slip of ~1.5 m of right lateral and 2 m of reverse slip along the London Hills Fault at Cape Campbell. Along the Fidget Fault, where clear discontinuities can be observed in the ALOS-2 descending interferogram and in ground observations, we obtained slip of ~6 m at a depth of ~10 km equating to a Mw 7.1 earthquake by itself.

Given the proximity of the event and the location of the southern end of the Hikurangi subduction zone, it is possible that some of the deep slip could be a result of slip on the interface which is located ~25 km beneath Kaikōura. To quantify the amount of slip which may have occurred we include an additional source to represent the subduction interface. The interface is modelled as a single plane which approximates the location of the subduction geometry in the area (19). In order to prevent large increases in moment from unrealistic slip on offshore regions of the interface not constrained by the data, we add moment constraint to the inversion limiting the total moment to an Mw 7.9 (assuming a shear modulus of 30 GPa). Although the addition of a subduction source does not significantly change the total misfit (< 1%), it is able to reproduce some of the subsidence inland which the crustal model alone cannot and the moment tensor is more similar to global moment tensor solutions (Figure 5). However, because of trade-offs between slip on the crustal faults and interface the model does introduce some larger misfits in the nearfield around the Kekerengu fault. The interface model predicts reverse slip of ~4 m at the base of the crustal faults inland of Kaikōura extending to the north where it decreases to ~1 m (Figure 6). On the crustal faults, the overall pattern of slip stays the same with maximum slip occurring along the Kekerengu segments. Across all of the modeled crustal faults slip is generally

shifted to shallower depths resulting a decrease in slip of ~ 4 m between 15 and 25 km depth and an increase, most notably on the Jordan Thrust and Kekerengu faults, of 3-4 m in the upper 10 km (Figure 6d). While the interface source helps to explain the observed farfield subsidence and non double-couple components of global moment tensors, the majority of moment is being generated by slip along the crustal faults (Table S2). In the case where we constrain the moment to a Mw 7.9, the contribution of the interface source is $\sim 15\%$. This drops to 2% if the magnitude is limited to an Mw 7.8 but increases to 29% in the case of an Mw 8.0.

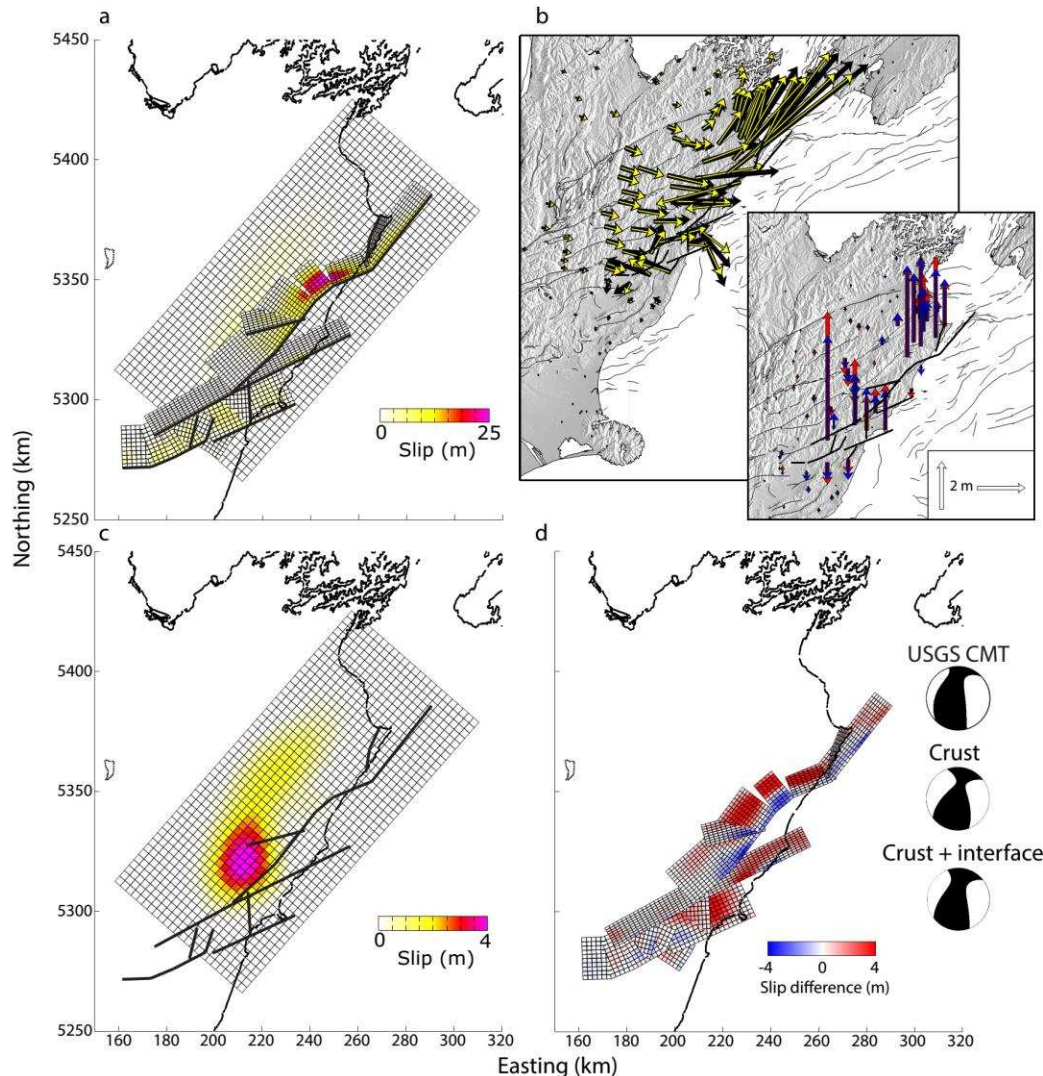


Figure 6: Best fitting slip model including an interface source. **a)** Best fitting slip models for the Kaikōura earthquake with the inclusion of an interface source. **b)** Observed and modelled surface displacements at continuous and campaign GPS based on the interface model. **c)** Slip distribution for only the interface, black lines show the location of the corresponding crustal faults shown in **a**. **d)** Difference in slip on the crustal faults when including the subduction interface as a source. Blue colors show areas where more slip is predicted by the interface model and red areas where more slip is predicted by the crustal only model. Moment tensors are for USGS CMT and two fault models for comparison.

Using both our best fitting source models described above, we modeled the tsunami wave field and compared it with the time series from marigrams from tide gauge stations at Kaikōura, Castlepoint, Wellington and Christchurch (Figure S3). The tsunami model used for this simulation was Comcot (32) which calculates the tsunami wave field propagation on a set of staggered regular grids solving the linear and non-linear shallow water wave equations. The relevant grid resolution was 0.5' in longitude and a maximum of 0.4' in latitude.

This source model explains the travel times to the individual tide gauge stations well, but shows discrepancies in wave amplitudes and wave phases (Figure S3). Amplitudes are generally too small, which is most pronounced for the Wellington and Christchurch marigrams. In Wellington the amplitude mismatch is a factor of ten and in Christchurch is a factor of five. Kaikōura and Castle point show a much better amplitude match with less than a factor of two mismatch. The observed mismatch may be due to local effects around the tide gauges (Wellington tide gauge for example is located inside the Wellington Harbour), a lack of detail in the bathymetry grids used for the simulation or it may indicate additional offshore deformation due to fault movement not identified in the inversion of onshore deformation. Alternatively, the contribution of horizontal displacements to the displacement of topography may be particularly important when there is such a large strike-slip component of slip (33). Interestingly, there is very little difference to the data fit when using either the crustal fault model or the model with an interface source. Because all of our currently available observations are onshore, both inversions produce very similar patterns of uplift which ultimately drive the tsunami simulations. A possible explanation is that we are missing slip offshore which we are unable to constrain with our subaerial observations alone.

Discussion and Conclusions

The Mw 7.8 Kaikōura earthquake clearly demonstrates that fault systems can undergo ruptures involving slip along numerous faults with diverse orientations, slip directions and degree of mechanical linkages. Geometric complexities have been suggested as a major control on the termination of a rupture (1-3). The exceptional rupture complexity during the Kaikōura earthquake, including apparent step overs of 15-20 km, would not have been considered as a plausible scenario in seismic hazard models. Moreover, the complex nature and lengthy propagation of the rupture hampered accurate early magnitude determination and would have posed issues for conventional earthquake early warning systems. While the faults to the north, including the Needles, Kekerengu, Jordan Thrust, and Upper Kowhai faults form a reasonably continuous structure, the distance between the Humps and Hundalee faults in the epicentral region and the Upper Kowhai and Hope faults is ~15 km. This gap coincides with a change from more reverse faulting in the south to predominantly strike slip in the north and is more than double the distance usually assumed as the limit for halting a fault rupture in standard seismic hazard models. The 2010 Mw 7.2 El Mayor-Cucapah in northern Mexico ruptured across a 10 km step-over in the surface faults, but gradients in optical pixel offsets and InSAR data indicated that slip continued at depth (7,34). During the Kaikōura earthquake, slip along the interface could also act as a linking structure at depth. However, models suggest that any slip on the interface was too far down to link Humps and Hundalee faults with the faults to the north. InSAR observations and subsequent field evidence suggest previously unmapped, north-south

striking faults, running between the Hundalee and Upper Kowhai fault (Figure 1) which might act as a transfer fault linking the two structures (Figures 4, 5). Given the variability in fault orientations, it is possible that this rupture could be explained by the keystone fault hypothesis whereby interlocking complex fault networks enable differential stresses to rise beyond the limit defined by optimally-oriented faults allowing a rupture to spontaneously propagate through an array of faults with a range of orientations (9). However, identifying which of the faults is the keystone fault will require further work. Regardless of the rupture mechanism, considering the incompleteness of many global fault databases, which typically only show surface faults, these observations highlight the need to account for larger jumps in hazard models which may be accommodated by unmapped faults or dynamic triggering (5, 6, 35).

Based on the location of the epicenter in the south and peak slip occurring much further north on the Kekerengu Fault, it is clear that the rupture initiated in the south and propagated north. We suggest that the earthquake's northward propagation onto numerous faults was the result of static stress changes imposed by the earlier stages of the rupture although dynamic stressing may also have played a role (34). Using only the fault slip from The Humps and Hundalee faults in the south, we calculate positive static stress changes (29) over much of the Upper Kowhai Fault and Jordan Thrust up to ~ 0.75 MPa (Figure 7). Large negative stress changes are predicted along much of the modelled Hope Fault. Localized areas of positive stress changes are modelled near on the inland portion of the Hope fault in addition to the offshore seaward end. We also assess stress changes on the northernmost faults (Kekerengu and Needles) due to slip on the Upper Kowhai Fault, Jordan Thrust and other faults further south. This indicates that the upper 10-15 km of the Kekerengu Fault was loaded by more than 2 MPa in regions where we estimate the largest coseismic slip. As a result of stressing by the Humps and Hundalee segments, large stress increases are also predicted in the area of maximum slip near the base of the Jordan Thrust (Figure 6). Using all of the crustal faults to stress the interface source shows large regions of increased stresses including an area offshore between Kaikoura and the Papatea fault consistent with the location of a cluster of aftershocks (Figure 1, 7, S1). Forward stressing of fault segments along the Kaikōura coast may have played an instrumental role in allowing the rupture to propagate along such a great length of the plate boundary.

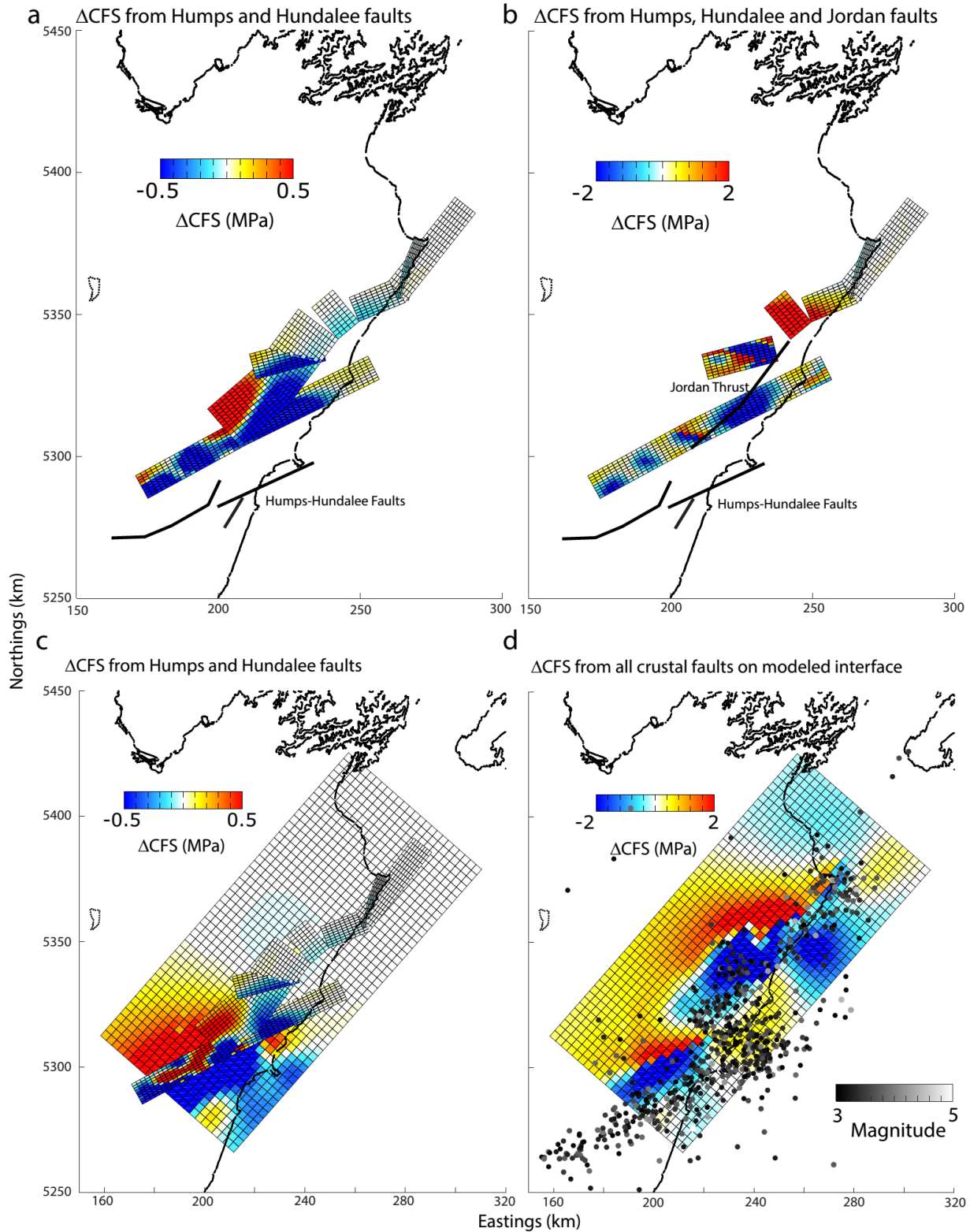


Figure 7. Predicted change in Coulomb stress along the modelled fault planes. **a)** CFS calculated on northern fault segments as a result of the estimated slip on The Humps-Hundalee faults in the south, shown by the heavy black lines. **b)** CFS on the northern fault segments as a result of the estimated slip on The Humps-Hundalee Faults and Jordan Thrust. **c)** CFS induced by the Humps

and Hundalee faults for the interface model. **d)** Stress change along the modelled interface as a result of slip along all of the crustal faults in the model. Circles indicate the location of aftershocks, as shown in Figure 1, color coded by magnitude.

Zones of permanent deformation are well documented in the geological record at step-overs in strike-slip fault zones at spatial scales of hundreds of meters or more (36-38). Large misfits to geodetic data observed following large earthquakes have also been explained by the occurrence of inelastic deformation and coseismic ground damage (39). Although our slip models can explain ~95% of the data variance, we are unable to account for a significant amount of the nearfield deformation. Some of the misfit, particularly in The Humps Fault Zone in the south, may be due to ground damage as suggested by the large reduction in coherence (Figure S6) between pre and co-earthquake interferograms. However, the large coherent uplift associated with the Papatea Fault and the anticlockwise rotation of the Papatea block (Figures 4, 8) suggests a significant component of rigid block motion. Given the complex fault configuration around the uplifted region which is bounded on the east by the westward-dipping Papatea Fault, to the west by the northwestward dipping Jordan Thrust and to the south by the northward dipping Hope Fault, it is difficult to fit the observed coseismic deformation using elastic dislocation methods. Based on the magnitude of the observed offset along the Papatea Fault which reaches almost 8 m, using elastic dislocations one would expect to see at least 4-5 m of subsidence on the footwall, yet we observed only 10s of centimeters of subsidence. To the west, the uplifted region lies within the footwall of the Jordan Thrust which should have subsided given the 2-3 m of uplift associated with the Jordan Thrust. This demonstrates that dislocation models struggle to reproduce the transfer of coseismic slip through complex fault networks or the asymmetric uplift and subsidence patterns around faults. The fault configuration around the uplifted block, asymmetric uplift pattern (40) and larger scale MFS is consistent with this structure being part of a pop-up structure within a restraining bend between the Jordan Thrust and Kekerengu Faults. Furthermore, a semi-continuous GPS installed within the Papatea block within two days of the earthquake shows negligible vertical post-seismic displacements and there have been no aftershocks associated with the lineament (Figure 4). The large right-lateral slip along the Upper Kowhai, Jordan Thrust and Kekerengu Faults on its northern boundary, compared with the negligible slip on the Hope Fault to the south, produces the observed anti-clockwise rotation (Figure 8). The narrowing of the stepover to the south and the presence of the steeply dipping Papatea Fault focusses uplift along the eastern edge of the block. It is also plausible that the Papatea fault changes dip and merges into the Hope Fault and Jordan thrust at shallow depths, and that the deformation and uplift of this block is a shallow feature. The magnitude of uplift within the block suggests that these pop-up structures can be created rapidly during large earthquakes. However, given the large coseismic displacements, the current topography and short repeat interval for events on the Kekerengu Fault and Jordan Thrust (390 years, 41), it is unlikely that this structure is activated during every earthquake. We suggest that much of its growth takes place only during larger multi-fault ruptures such as the 2016 Kaikōura earthquake which propagate through the restraining stepover.

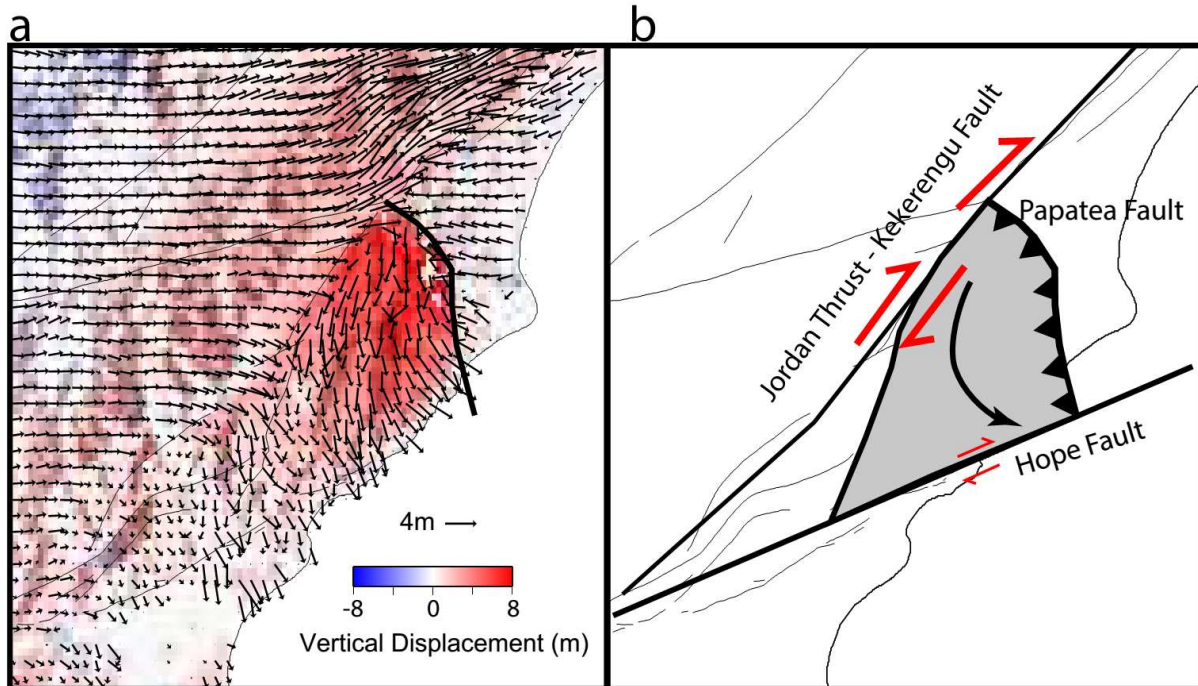


Figure 8: a) 3D displacement field over the Papatea block. The arrows show the horizontal displacements as shown in Figure 3 and the background shows the vertical displacements. b) Schematic diagram explaining the cause of the anticlockwise rotation of the block (see main text).

The depths to which faults slip has important implications for seismic hazard. Observations from large earthquakes show an increase in average slip with increasing fault length in excess of the length scale set by the seismogenic thickness (42-44). Though not observed, this would imply higher stress drops for larger events. To reconcile this, models have been put forward which suggest deep slip which penetrates the base of the seismogenic layer (42,43). Many of the faults in the Kaikoura earthquake have significant modelled slip to depths approaching 25 km, even in the event of slip along the interface slip of 4-5 m is required. This is much greater than rupture depths prescribed in the New Zealand National Seismic Hazard Model (12-15 km, 41). While the resolution of the model will be reduced at depth, tests where we vary the bottom depth from 15-30 km shows an increase in the residuals when the bottom depths are less than 25 km. The deeper seismogenic depths that we observe in our best-fitting models may be due to the cooling effect of the subducting Hikurangi slab, which will deepen a thermally controlled brittle to ductile transition.

Paleoseismological data is widely used for informing recurrence intervals for individual faults in seismic hazard models (41). However, if an event with this level of complexity would have happened in the past it would likely have been interpreted as multiple events biasing estimates of maximum magnitude and recurrence interval. This, combined with the large apparent fault jumps between some of the fault ruptures, would preclude the Kaikoura earthquake as a scenario earthquake in even the most well-developed seismic hazard models (10). While the

unprecedented, complex, multi-fault rupture observed in the Kaikoura earthquake may in part be related to the geometrically complex nature of the faults in this region, this event emphasizes the importance of re-evaluating how rupture scenarios are defined for seismic hazard models in plate boundary zones worldwide.

References

1. S. G. Wesnousky, Predicting the endpoints of earthquake ruptures. *Nature*, 444(7117), pp.358-360 (2006)
2. S.G. Wesnousky, Displacement and geometrical characteristics of earthquake surface ruptures: Issues and implications for seismic-hazard analysis and the process of earthquake rupture. *Bulletin of the Seismological Society of America*, 98(4), pp.1609-1632 (2008)
3. A. A. Barka, K. Kadinsky-Cade, Strike-slip fault geometry in Turkey and its influence on earthquake activity. *Tectonics*, 7(3), pp.663-684 (1988)
4. G. P. Biasi, S. G. Wesnousky, Steps and Gaps in Ground Ruptures: Empirical Bounds on Rupture Propagation. *Bulletin of the Seismological Society of America* (2016)
5. C. Pagli, R. Pedersen, F. Sigmundsson, K. L. Feigl, Triggered fault slip on June 17, 2000 on the Reykjanes Peninsula, SW-Iceland captured by radar interferometry. *Geophysical Research Letters*, 30(6) (2003)
6. E. Nissen et al, Limitations of rupture forecasting exposed by instantaneously triggered earthquake doublet. DOI: 10.1038/NCEO2653, *Nature Geoscience* (2016)
7. J. M. Fletcher et al, Assembly of a large earthquake from a complex fault system: Surface rupture kinematics of the 4 April 2010 El Mayor–Cucapah (Mexico) Mw 7.2 earthquake. *Geosphere* 10, 797–827 (2014)
8. J. M. Fletcher, M. E. Oskin, O. J. Teran, The role of a keystone fault in triggering the complex El Mayor–Cucapah earthquake rupture. 9, 303–307. doi:10.1038/ngeo2660 *Nature Geoscience* (2016)
9. J. Beavan, M. Motagh, E. J. Fielding, N. Donnelly, D. Collett, Fault slip models of the 2010–2011 Canterbury, New Zealand, earthquakes from geodetic data and observations of postseismic ground deformation. *New Zealand Journal of Geology and Geophysics*, 55(3), 207-221. (2012)
10. E. H. Field et al, Uniform California Earthquake Rupture Forecast, Version 3 (UCERF3): The time-independent model. *B. Seismol. Soc. Am.* 104, 1122–1180 (2014)
11. R. M. Langridge et al, The New Zealand Active Faults Database. *New Zealand Journal of Geology and Geophysics*; 59(1):86-96 (2016)
12. N. J. Litchfield et al, A model of active faulting in New Zealand. *New Zealand Journal of Geology and Geophysics*, 57(1), pp.32-56 (2014)
13. J. Beavan et al, New Zealand GPS velocity field: 1995–2013. *New Zealand Journal of Geology and Geophysics*, 59(1), pp.5-14 (2016)

14. A. Nicol, J. Beavan, Shortening of an overriding plate and its implications for slip on a subduction thrust, central Hikurangi Margin, New Zealand. *Tectonics*, 22(6). (2003)
15. L. M. Wallace, J. Beavan, R. McCaffrey, D. Darby, Subduction zone coupling and tectonic block rotations in the North Island, New Zealand. *Journal of Geophysical Research: Solid Earth*, 109(B12) (2004)
16. R. J. Norris, A. F. Cooper, Late Quaternary slip rates and slip partitioning on the Alpine Fault, New Zealand. *Journal of Structural Geology*, 23(2), pp.507-520 (2001)
17. W. E. Holt, A. J. Haines, The kinematics of northern South Island, New Zealand, determined from geologic strain rates. *Journal of Geophysical Research: Solid Earth*, 100(B9), pp.17991-18010 (1995)
18. J. R. Pettinga, M. D. Yetton, R. J. Van Dissen, G. Downes, Earthquake source identification and characterisation for the Canterbury region, South Island, New Zealand. *Bulletin of the New Zealand National Society for Earthquake Engineering*, 34(4), pp.282-317. (2001)
19. C. A. Williams et al, Revised interface geometry for the Hikurangi subduction zone, New Zealand. *Seismological Research Letters*, 84(6), pp.1066-1073. (2013)
20. L. M. Wallace et al, Balancing the plate motion budget in the South Island, New Zealand using GPS, geological and seismological data. *Geophysical Journal International*, 168(1), pp.332-352 (2007)
21. A. M. Benson et al, Late Quaternary paleoseismic history and surface rupture characteristics of the eastern Awatere strike-slip fault, New Zealand. *Geological Society of America Bulletin*, 113(8), pp.1079-1091 (2001)
22. J. Zachariassen et al, Timing of late Holocene surface rupture of the Wairau fault, Marlborough, New Zealand. *New Zealand Journal of Geology and Geophysics*, 49(1), pp.159-174 (2006)
23. R. Van Dissen, A. Nicol, Mid-late Holocene paleoseismicity of the eastern Clarence Fault, Marlborough, New Zealand. *New Zealand Journal of Geology and Geophysics*, 52(3), pp.195-208 (2009)
24. R. Van Dissen, R. S. Yeats, Hope fault, Jordan thrust, and uplift of the seaward Kaikoura Range, New Zealand. *Geology*, 19(4), pp.393-396.(1991)
25. P. L. Knuepfer, Temporal variations in latest Quaternary slip across the Australian-Pacific plate boundary, northeastern South Island, New Zealand. *Tectonics*, 11(3), pp.449-464 (1992)
26. R. M. Langridge, K. R. Berryman, Morphology and slip rate of the Hurunui section of the Hope Fault, South Island, New Zealand. *New Zealand Journal of Geology and Geophysics*, 48(1), pp.43-57 (2005)
27. I. J. Hamling et al, Crustal deformation and stress transfer during a propagating earthquake sequence: The 2013 Cook Strait sequence, central New Zealand. *Journal of Geophysical Research: Solid Earth*, 119(7), pp.6080-6092 (2014)

28. J. Ristau, Update of regional moment tensor analysis for earthquakes in New Zealand and adjacent offshore regions. *Bulletin of the Seismological Society of America*, 103(4), pp.2520-2533. (2013)
29. Materials and Methods are available as supplementary materials on Science Online
30. Y. Okada, Surface deformation due to shear and tensile faults in a half-space. *Bulletin of the seismological society of America*, 75(4), pp.1135-1154 (1985)
31. R. Bro, S. De Jong, A fast non-negativity-constrained least squares algorithm. *Journal of chemometrics*, 11(5), pp.393-401 (1997)
32. X. Wang, W. Power, COMCOT: A tsunami generation propagation and run-up model, GNS Science consultancy report 2011/43, GNS Science, Lower Hutt, New Zealand (2011)
33. A. Hooper et al, Importance of horizontal seafloor motion on tsunami height for the 2011 M_w= 9.0 Tohoku-Oki earthquake. *Earth and Planetary Science Letters*, 361, pp.469-479. (2013)
34. M. -H. Huang et al, Fault Geometry and Slip Distribution of the 2010 Mw 7.2 El Mayor-Cucapah Earthquake from Geodetic Data, *Journal of Geophysical Research*, doi:10.1002/2016JB012858. (2017)
35. W. Fan, P. M. Shearer, Local near instantaneously dynamically triggered aftershocks of large earthquakes. *Science*, 353(6304), pp.1133-1136 (2016)
36. Y. Fialko et al, Deformation on nearby faults induced by the 1999 Hector Mine earthquake. *Science*, 297(5588), pp.1858-1862 (2002)
37. O. Dor, Y. Ben-Zion, T. K. Rockwell, J. Brune, Pulverized rocks in the Mojave section of the San Andreas Fault Zone. *Earth and Planetary Science Letters*, 245(3), pp.642-654 (2006)
38. Y. Kaneko, Y. Fialko, Shallow slip deficit due to large strike-slip earthquakes in dynamic rupture simulations with elasto-plastic off-fault response. *Geophysical Journal International*, 186(3), pp.1389-1403 (2011)
39. R. E. Reilinger et al, Coseismic and postseismic fault slip for the 17 August 1999, M= 7.5, Izmit, Turkey earthquake. *Science*, 289(5484), pp.1519-1524 (2000)
40. M. R. Legg et al, Morphology, structure and evolution of California Continental Borderland restraining bends. *Geological Society, London, Special Publications*, 290(1), pp.143-168 (2007)
41. M. Stirling et al, National seismic hazard model for New Zealand: 2010 update. *Bulletin of the Seismological Society of America*, 102(4), pp.1514-1542 (2012)
42. C. Scholz, Scaling laws for large earthquakes: consequences for physical models, *Bull. Seismol. Soc. Am.* 72, 1-14 (1982)
43. G. C. King, S. G. Wesnousky, Scaling of fault parameters for continental strike-slip earthquakes. *Bulletin of the Seismological Society of America*, 97(6), pp.1833-1840 (2007)

44. B. E. Shaw, S. G. Wesnousky, Slip-length scaling in large earthquakes: The role of deep-penetrating slip below the seismogenic layer. *Bulletin of the Seismological Society of America*, 98(4), pp.1633-1641 (2008)
45. Y. Shokin, L. B. Chubarov, V. A. Novikov, A. N. Sudakov, Calculations of tsunami travel time charts in the Pacific Ocean, *Science of Tsunami Hazards*, vol. 5, p. 85-113 (1987)
46. C. Liang, E. J. Fielding, Interferometry with ALOS-2 full-aperture ScanSAR data, *IEEE Trans. Geosci. Remote Sens.*, in revision (2016)
47. C. Liang, E. J. Fielding, Measuring azimuth deformation with L-band ALOS-2 ScanSAR interferometry, *IEEE Trans. Geosci. Remote Sens.*, (2016)
48. P. A. Rosen, E. Gurrola, G. F. Sacco, H. Zebker, The InSAR scientific computing environment, *Proc. EUSAR*, Nuremberg, Germany, Apr. 23–26, 2012, 730–733 (2012)
49. R. M. Goldstein, C. L. Werner, Radar interferogram filtering for geophysical applications. *Geophysical Research Letters*, 25(21), pp.4035-4038 (1998)
50. C. W. Chen, H. A. Zebker, Phase unwrapping for large SAR interferograms: Statistical segmentation and generalized network models. *IEEE Transactions on Geoscience and Remote Sensing*, 40(8), pp.1709-1719 (2002)
51. T. G. Farr et al, The shuttle radar topography mission. *Reviews of geophysics*, 45(2). Farr, T. G., P. A. Rosen, E. Caro, R. Crippen, R. Duren, S. Hensley, et al., The shuttle radar topography mission, *Reviews of Geophysics*, 45, (2007).
52. T. Herring, R. King, S. McClusky, Introduction to GAMIT/GLOBK, Release 10, p. 571, Mass. Inst. of Tech., Cambridge, U. K (2010)
53. B. Parsons et al, The 1994 Sefidabeh (eastern Iran) earthquakes revisited: new evidence from satellite radar interferometry and carbonate dating about the growth of an active fold above a blind thrust fault. *Geophys. J. Int.* 164, 202–217 (2006)
54. P. Segall, Integrating geologic and geodetic estimates of slip rate on the San Andreas fault system. *Int. Geol. Rev.* 44 (1), 62–82 (2002)
55. I. J. Hamling et al, Stress transfer between thirteen successive Dyke intrusions in Ethiopia. *Nature Geoscience*. 3, 713–717 (2010)

Acknowledgments: The authors would like to thank JAXA for access to ALOS-2 data, the EU Copernicus and the European Space Agency for access to and scheduling of Sentinel-1 data, and GeoNet (<http://geonet.org.nz>), PositionNZ, AllTerra, Eliot Sinclair, Global Survey and IGS for GPS data. We would also like to thank the all of the people who helped collect data from the field. We acknowledge the use of bathymetry data for tsunami travel time and propagation modelling from Land Information New Zealand, the National Institute of Water and Atmospheric Research, Seabed Mapping International, the National Geophysical Data Centre and the General Bathymetric Chart of the Oceans

Author Contributions: IJH carried out the elastic modeling and led the writing of the paper with help from TJW, LMW, SH, and contributions from all authors. JRE, EJF and CL acquired and processed the InSAR datasets. SH estimated the GPS coseismic offsets and KC led the collection and analysis of the coastal uplift data. NP, PD and SH organized and led the campaign GPS field work with support from with additional support from Land Information New Zealand (LINZ) and Otago University. SB analyzed

and provided the relocated earthquake catalogue. NL and PV led the surface faulting work and CM, DB and WP analyzed and modelled tsunami data. **Funding:** This work was supported by public research funding from the Government of New Zealand with additional support from LINZ. JRE and TJW were funded by the Royal Society and UK NERC through the Centre for the Observation and Modelling of Earthquakes, Volcanoes and Tectonics (COMET) and grant NE/K010867/1. Part of this research was carried out at the Jet Propulsion Laboratory (JPL), California Institute of Technology, under a contract with the National Aeronautics and Space Administration (NASA Earth Surface and Interior focus area). Cunren Liang was also supported by an appointment to the NASA Postdoctoral Program at JPL. The ALOS-2 original data are copyright Japan Aerospace Exploration Agency (JAXA) and provided under JAXA RA4 PI Project P1372002. **Competing Interests:** The authors declare that they have no competing interests. **Data and materials availability:** All data needed to evaluate the conclusions in the paper are present in the paper and/or the Supplementary Materials. Additional data available from the authors upon request.